Advantages of Inter-calibration for Geostationary Satellite Sensors onboard Twin Satellites

Yeeun Lee[1], Myoung-Hwan Ahn[1], Mina Kang[1], Mijin Eo[1], Dohyeong Kim[2], Kyung-Jung Moon[3]

[1]Department of Climate and Energy Systems Engineering, Ewha Womans University, Seoul, Republic of Korea

[2]National Meteorological Satellite Center, Korea Meteorological Administration, Jincheon, Republic of Korea

[3]National Institute of Environmental Research, Incheon, Republic of Korea

Corresponding author: Myoung-Hwan Ahn (terryahn65@ewha.ac.kr)

Key Points:

- Inter-calibration based on ray-matching between geostationary satellite sensors onboard twin satellites.
- Implementation of collocation process in the visible wavelengths and the application of weighted statistics for ensuring collocation stability.
- The novel advantages of the GEO-GEO inter-calibration approach for future applications

Abstract

To address the increasing demand for diurnal information on trace gases and aerosols, a series of geostationary (GEO) satellite programs called GEO-constellation have been initiated, with the launch of the Geostationary Environment Monitoring Spectrometer (GEMS) onboard Geostationary Korea Multi-Purpose Satellite 2B (GK2B). To assess the sensor performance of GEMS in orbit, the current work suggests employing an inter-calibration methodology involving the Advanced Meteorological Imager (AMI) aboard its twin satellite, GK2A. Twin satellites have a significant advantage in obtaining collocation datasets across diverse spatiotemporal conditions, enabling rigorous collocation criteria effectively reducing mismatch uncertainty. The collocation results present robust correlation coefficients over 0.98, revealing the current calibration characteristics of the sensors. This research emphasizes the advantages of the GEO-GEO inter-calibration, particularly the capability of analyzing spatial and temporal dependencies. These findings confirm the mutual benefit of utilizing the sensors in similar configurations, highlighting their importance for future satellite monitoring endeavors.

Plain Language Summary

Understanding the daily changes in air pollutants is crucial for grasping how these substances move and disperse in the air, aiding efforts to reduce pollution. In this regard, satellites have a distinct advantage in observation owing to their wide spatial coverage at regular intervals. GEMS is one of the geostationary sensors providing such information for the Asia-Pacific region nearly 7-8 times a day. To evaluate the reliability of GEMS, this study proposes an inter-calibration method by comparing GEMS observations with those of AMI aboard GK2A. These satellites have a unique advantage as they fly close to each other, observing the Earth with matched optical viewing paths. Scenes simultaneously observed by AMI and GEMS exhibit strong agreement, thus revealing the inherent observation characteristics of each sensor. These findings confirm the mutual benefit of utilizing the sensors in similar configurations for satellite monitoring during the operation.

1 Introduction

A global network of geostationary (GEO) satellites for air quality monitoring is to be established soon, including the Geostationary Environment Monitoring Spectrometer (GEMS), Tropospheric Emissions: Monitoring of Pollution (TEMPO) and Sentinel-4 over East Asia, Northern America, and Europe, respectively. These GEO satellite sensors measure specific areas multiple times a day, which gives a significant advantage in providing diurnal information on trace gases and aerosol properties (J. Kim et al., 2020; Zoogman et al., 2017). The observations obtained from the GEO constellation will be crucial for monitoring the long-range transport of air pollutants and changes in pollutant levels throughout the day. However, the effective utilization of the measurements relies on the capability to ensure consistency in measurements across sensors having varying designs, specifications, and calibration processes. This underscores the need for implementing measures to monitor measurement quality throughout their operational period.

In this regard, inter-calibration has been an effective measure for post launch calibration (Chander et al., 2013). Especially for GEO sensors, ray-matching with low Earth orbit (LEO) satellite sensors has been widely applied, considering that LEO sensors cover different field of regards (FOR) of various GEO imagers (Doelling et al., 2016; Jiang et al., 2009; Minnis et al., 2002a, 2002b). Ray-matching between GEO-GEO sensors, however, has not been fully investigated as the FORs of GEO sensors cover distinct regions, like in the case of GEMS and TEMPO. The characteristic has led to the development of inter-calibration for the GEO sensors through intermediary means (Chander et al., 2013), such as radiative transfer models (Alsweiss et al., 2015), transfer measurements (L. Wang et al., 2009), or numerical weather prediction models (S. J. Lee & Ahn, 2021; Saunders et al., 2013).

However, there is a unique circumstance where direct GEO-GEO comparison becomes feasible especially when the sub-nadir satellite longitudes of the spacecrafts are exceptionally close. The onboard sensors in this condition observe Earth scenes with coincident optical viewing paths, which greatly reduces collocation mismatch. Luckily, GEMS onboard the Geostationary Korea Multi-Purpose Satellite-2B (GK2B) has a corresponding pair satisfying the condition, the Advance Meteorological Imager (AMI) onboard its twin satellite, GK2A. It is facilitated because the two satellites are positioned within a 0.05° control box centered around 128.2°E longitude.

Collocation between the sensors is straightforward and has several advantages such as: (1) the huge number of collocated samples; (2) full coverage of solar and viewing angles; and (3) wide spatiotemporal coverage. With the advantages, here we focus on optimizing the collocation conditions and further clarify the current calibration issues of the sensors through spatial and temporal analyses. If possible, GEMS and AMI could serve as useful sources for understanding the observation characteristics of the sensors during their operational periods, in terms of relative standards. Additionally, the GEO-GEO comparison can serve as a high-quality collocation reference for GEO-LEO collocation, given the strictest collocation criteria.

2 Data and Methods

2.1 Sensor specification

2.1.1 GEMS

GEMS scans the Asia-Pacific region (5°S-45°N, 75-145°E) in the east-west direction by moving a scan mirror, while maintaining a fixed north-south field of view of about 7.78° (Choi et al., 2019; J. Kim et al., 2020). GEMS is designed to measure spectral radiances ranging from 300 to 500 nm (Level 1B) with a spectral resolution of better than 0.6 nm. To monitor and calibrate the Level 1B products, two transmissive solar diffusers and light emitting diode (LED) are deployed as the on-board calibration system. Alongside this system, monitoring and calibration methods have been devised and performed with various statistical approaches since the completion of the in-orbit test in October 2020 (Kang et al., 2020, 2022; Y. Lee et al., 2020).

The assessment has revealed a significant calibration issue in GEMS solar observations, specifically associated with spatial dependence along the north-south direction. The dependence is attributed to the unresolved azimuth angle dependence in the bidirectional transmittance distribution function (BTDF) of the solar diffusers (Kang et al., 2023). Theoretically, the dependence should specifically impact solar irradiance but not Earth radiance. This distinction originates from the shared optical paths within the instrument for both solar and Earth observation modes, except for the solar diffusers. To confirm the cause of the dependence, it is necessary to ensure that the Earth's radiance is not affected by this. However, radiances observing various Earth scenes make it challenging to discern the dependence originating from the BTDF. In this situation, inter-calibration with AMI emerges as a useful means to evaluate the issue, given that the collocation datasets can perfectly cancel out the scene variabilities. To validate this, we employ the upgraded version (provisional) of GEMS solar irradiance and evaluate the BTDF correction (refer to Section 3.1) along with addressing other calibration concerns.

2.1.2 AMI

AMI has six visible/near infrared and ten infrared channels for continuous atmospheric monitoring. The first visible channel at a central wavelength of 470 nm (Ch01) is employed for the comparison since the spectral response function (SRF) of the channel is fully encompassed by the GEMS observations. To obtain surface information, an infrared channel centered at 10.5 μm (window channel, Ch13) is collocated together with Ch01. This study employs full-disk observations taken at ten-minute intervals for Ch0l and Ch13, with spatial resolutions of 1 and 2 km, respectively. For visible and near-infrared channels, the National Meteorological Satellite Center (NMSC) has applied multiple calibration techniques such as solar calibration with a solar diffuser, vicarious calibration using the radiative transfer model (RTM) over the Australian deserts, and ray-matching with the Moderate Resolution Imaging Spectroradiometer (MODIS) onboard Terra and Aqua and the Visible Infrared Imaging Radiometer Suite (VIIRS) onboard NOAA-20 and Suomi-National Polar-orbiting Partnership (Suomi-NPP). The calibration results (D. Kim et al., 2021) as well as the related information is well organized in the following website (URL: http://210.125.45.71/enhome/html/gsics/vicariousIntroGK2A.do).

2.2 Ray-matching

Ray-matching had been developed to relate measured information of GEO and LEO sensors in early days for the Clouds and the Earth's Radiant Energy System (CERES) project (Minnis and Harrison, 1984; Minnis et al., 1991). Afterwards, the concept of relating the GEO-LEO measurements has been employed to calibrate GEO imagers by setting a well-calibrated LEO sensor as a reference (Minnis et al., 2002a, 2008; Doelling et al., 2016; Xiong et al., 2020). Targeting specific scenes such as deep convective clouds (DCC) has been further developed as it can reduce the bidirectional reflectance distribution function (BRDF) effects of the clouds (Hu et al., 2004; Bhatt et al., 2017). Setting a particular target contributes to effectively detecting sensor-specific signals, while it reduces the number of datasets as a trade-off. To mitigate this, a statistical approach has been developed especially for the DCC calibration, and it has proven effective in detecting sensor degradation (Doelling et al., 2013).

In this study, we take advantage of ray-matching between AMI and GEMS, observing spatiotemporally matched scenes, all with coinciding optical viewing paths without requiring additional treatment. When empirically checking the position vectors of GK2A and GK2B over the course of a year, the angles between the position vectors in the Earth-cantered, Earth-fixed (ECEF) coordinates vary up to 0.06°. This variation introduces viewing angle differences approximately on the order of 0.01-0.1°, which is practically small compared to the current ray-matching condition between GEO-LEO, mostly 1% for the viewing zenith angle (VZA) differences (D. Kim et al., 2021). The advantage guarantees huge collocation datasets, facilitating further data filtering and a more rigorous spatiotemporal match, as detailed in the following sections.

2.2.1 Spatial, temporal, and spectral matching

Spatial averaging is applied to both sensor observations with a grid size of 0.1°. The spatial averaging can reduce random noise originated from natural variability and image navigation and registration (INR) uncertainty. In addition to the averaging, standard deviation is also derived for each grid to characterize scene inhomogeneity (Doelling et al., 2013). This inhomogeneity is closely related to collocation error and is further employed as weights in the weighted linear regression (refer to Section 2.3).

Temporal matching is performed by calculating the observation time difference for each grid. GEMS provides approximately 700 scan images for 30-minutes observation. During the GEMS observation, several AMI full-disk images are taken and pieced together with the temporal match threshold (Δt < 5 minutes). The time matching inherently aligns solar zenith angle (SZA) and solar azimuth angle (SAA) between the sensors without additional treatment.

Finally, the hyperspectral observations of GEMS are convolved with the AMI SRF for spectral matching. The convolved radiance and irradiance of GEMS are normalized by the sum of the SRF. The bidirectional reflectance is calculated after the convolution process as follows:

$$(1)\ R = \frac{\pi I}{\mu_0 F}$$

where F, I, R and μ_0 denotes the measured solar irradiance, Earth radiance, reflectance, and the cosine of SZA for the optical path length correction.

2.2.2 Filtering test

After the collocation process, the grids consisting of land and sun-glint pixels are screened out. Land scenes have higher natural variability increasing variances in radiance biases between AMI and GEMS. Sun-glint scenes corresponding to specular reflection seem to be more vulnerable to temporal mismatches, which could add a systematic bias depending on the observation time difference. The SZA and VZA are also limited to 60°, because the grids with larger zenith angles may have high collocation error caused by longer optical path lengths (Sterckx et al., 2013). Similarly, the longitudes are also constrained to values over 100°E, because the number of GEMS pixels within a grid box is very small (<4-5 pixels) in the far-western region in the GEMS FOR. The number of collocation datasets even after these filtering conditions is around 20,000-40,000 every hour, while the number varies with times and seasons.

2.3 Weighted linear regression

To obtain stable signals from the scenes ranging from dark ocean to very bright clouds, we employ weighted linear regression. The standard deviation mentioned in Section 2.2.1 serves as a weight for each collocated grid, increasing the contribution from highly homogeneous scenes in the statistics. The method has been widely applied to collect spatially homogeneous cloud tops (Doelling et al., 2013). However, the standard deviation tends to increase with brighter scenes, thereby reducing the contribution of the cloud scenes. To ensure equal contribution regardless of signal levels, the standard deviation of each grid is divided by the mean (Hewison, 2013), resulting in the relative uncertainty (v_i and w_i) as follows:

$$(2)\ v_i = u(X_i)^{-1} = \left(\frac{\sigma(X_i)}{m(X_i)}\right)^{-1} \text{ and } w_i = u(Y_i)^{-1} = \left(\frac{\sigma(Y_i)}{m(Y_i)}\right)^{-1}$$

where σ and m indicates the standard deviation and the mean of reflectances for each grid, respectively. The subscript i indicates the grid index in the collocation datasets and X_i and Y_i are the AMI and GEMS observations within the i-th grid. The weighted linear regression shows more stable results when accounting for the uncertainties associated with X_i and Y_i together. Empirically, the weighted regression presents a stable trend compared to non-weighted regression especially when the interval becomes shorter such as on a daily or hourly basis. The applied regression method with the weights is the generalized distance regression (GDR) introduced by the following document (ISO/TS 28037, 2010).

3 Results and Discussion

AMI and GEMS observations are collected over two years from November 2020 to May 2023 every hour during daytime. The datasets presented in Section 3.1 particularly undergo screening based on the spatial inhomogeneity condition ($u(X_i) < 5\%$ and $u(Y_i) < 5\%$). Figure 1 presents the collocation datasets measured in January and July 2021, showing the regression slopes larger than unity. The positive bias of GEMS will be discussed in detail in Section 3.2.1. The correlation presents a good agreement with the coefficients over 0.98 regardless of observation times and seasons. The GEMS radiances over 592.35 W cm^{-3} sr^{-1} are affected by saturation, resulting in the limiting feature for higher signals. Even after applying the scene homogeneity condition, the number of collocation datasets exceeds 1,500,000 every month. With the datasets, the following sections will present spatial and temporal analysis results between AMI and GEMS.

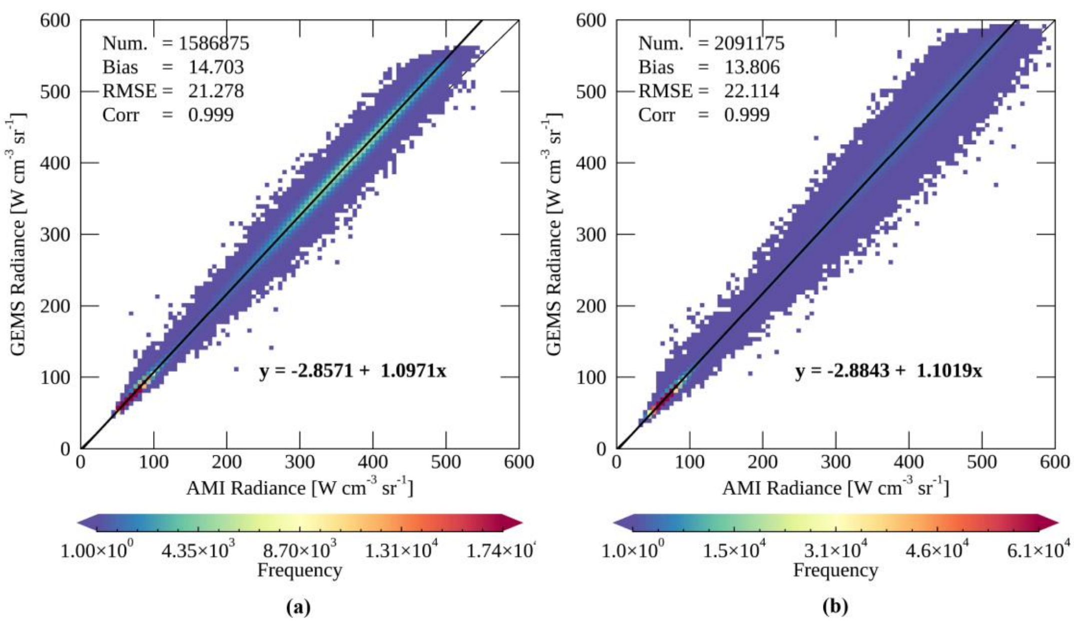

Figure 1. Scatter density plots of AMI and GEMS radiances measured in (a) January and (b) July 2021 (01-06 UTC) with statistics based on the weighted linear regression. The color bar indicates the number of collocation datasets after binning with the bin size of 1 W cm^{-3} sr^{-1}.

3.1 Spatial analysis

3.1.1 North-south spatial dependence

As mentioned earlier, a primary issue regarding GEMS Level 1B products was the north-south spatial dependence in solar irradiance, which is expected to show up in Earth reflectance. To verify this, mean biases of reflectance between AMI and GEMS are calculated with the collocation datasets measured in January and July 2021. Invalid grids including bad pixels around 10-15 °N latitudes are filtered out during the collocation process (Y. Lee et al., 2023). The north-south spatial dependence has seasonal variation, and it is clearly shown in Figure 2 (the first column) with the reversed pattern for different seasons. The BTDF correction updated by Kang et al. (2023) has greatly improved GEMS solar irradiance and, consequently, Earth reflectance. The second column in Figure 2 demonstrates the improvement with consistent trends across all latitudes. The update has effectively removed the north-south dependence, reducing biases in solar irradiance from approximately 20% to within 4%. Regarding reflectance, the biases converge to 15% across all latitudes.

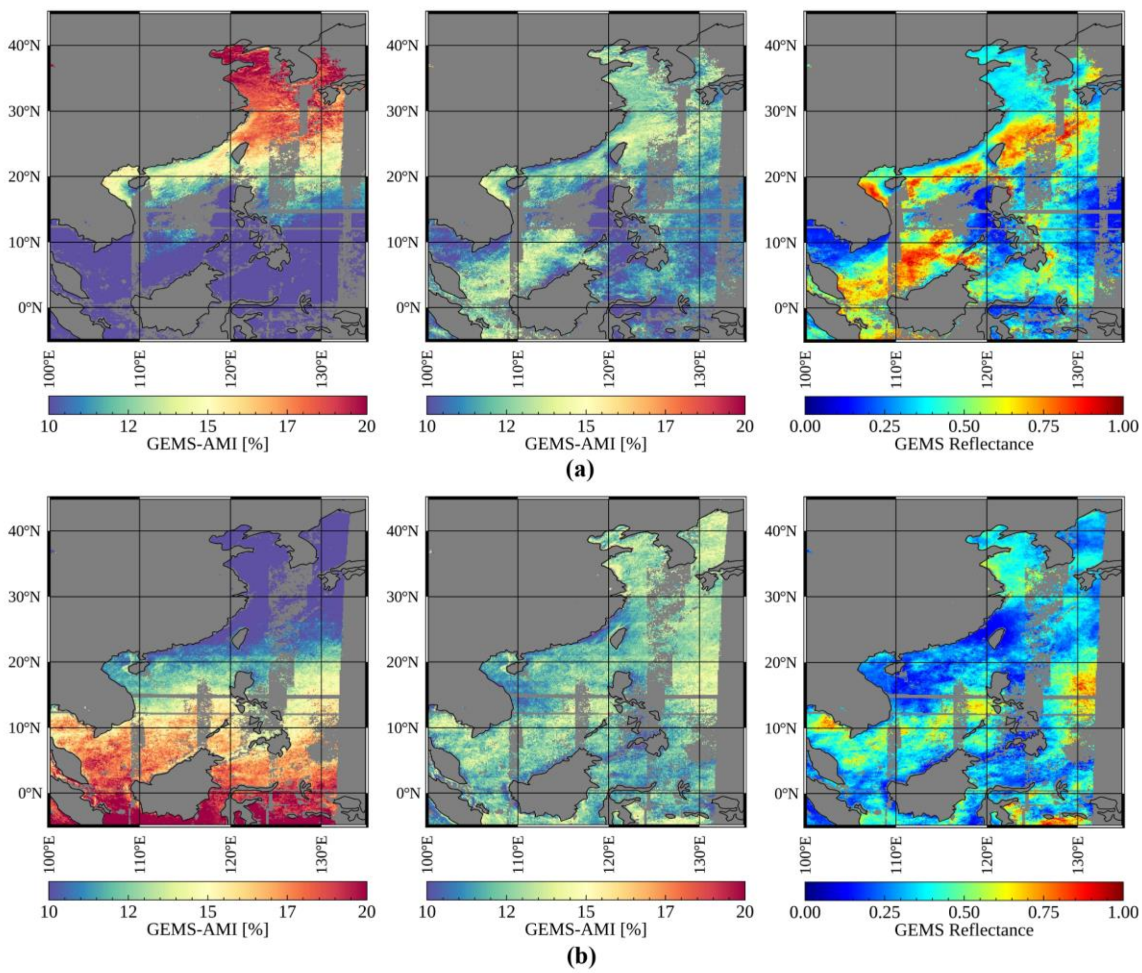

Figure 2. The mean biases in percentage between AMI and GEMS reflectances before (the first column) and after (the second column) the GEMS BTDF update. The third column presents mean reflectances of GEMS for each grid. The collocation datasets are the observations in (a) January and (b) July 2021 (01-06 UTC).

3.1.2 Signal dependence

Another finding in Figure 2 is the appearance of signal dependence after removing the north-south spatial dependence. Particularly for lower reflectances (below 0.4), the positive biases rapidly increase, as the signal levels increase. The dependence associated with lower reflectances is further investigated with the scattering angle as follows:

$$(3)\ cos\Theta = -cos\theta_0 cos\theta - sin\theta_0 sin\theta \cos(\phi_0 - \phi)$$

where $\Theta, \theta_0, \theta, \phi_0$ and ϕ represent the scattering angle, SZA, VZA, SAA, and viewing azimuth angle (VAA), respectively. In the visible spectral domain, Rayleigh scattering predominantly accounts for about 80% of the top of the atmosphere (TOA) reflectances, particularly over dark ocean (Sterckx et al., 2013; M. Wang, 2016). The scattering angle computed in Equation (3) determines the intensity of Rayleigh scattering, as the input parameter for the Rayleigh scattering phase function. The intensity generally increases when the direction approaches forward or backward scattering, corresponding to the angles of 0° or 180°, respectively.

Figure 3 depicts the scattering angle dependence for the collocation datasets having AMI reflectance lower than 0.3 and the brightness temperatures (Ch13) greater than 280 K. The selected datasets are grouped by scattering angles with the angle interval of 5°. In Figure 3a, the dependence on scattering angle is evidently clear, with the reflectance distributions decreasing for higher scattering angles. This is because the light observed at the TOA has been more scattered within the atmosphere under backscattering conditions. It should be noted that the effects of reflected light from ocean surfaces may exist, albeit with a smaller impact. The distributions having lower scattering angles exhibit higher mean biases as shown in Figure 3b, presenting consistent results with the signal dependence. This indicates that the signal and scattering angle dependencies might be intertwined, particularly for lower radiances. The potential cause of these dependencies is still unclear, but it needs to be clarified in further research since the scattering angle dependence could be mis-interpreted as temporal dependence. In other words, variations in scattering angles, influenced by the solar position, could lead to seasonal or diurnal fluctuations.

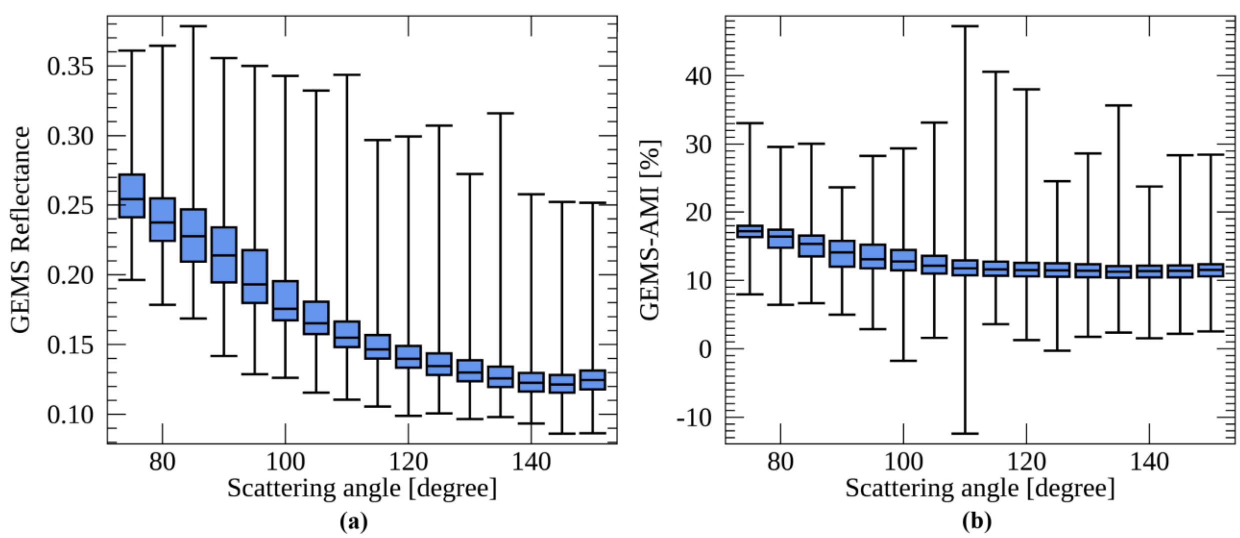

Figure 3. The box plots for dark ocean scenes of (a) GEMS reflectances and (b) the biases with AMI grouped by scattering angles with a class width of 5°.

3.2 Temporal analysis

The previous section analyzes dependencies based on geolocation variables, as collocation datasets cover a wide range of spatiotemporal conditions. This section focuses on temporal aspects of the collocation datasets collected at various observation intervals. For temporal analysis, the weighted regression is used due to the stable trends exhibited by the indicator.

3.2.1 Radiometric calibration

Figure 4 presents the regression slopes of AMI and GEMS, compared with the slopes between AMI and VIIRS (GEO-LEO) onboard Suomi-NPP and NOAA20 provided by NMSC. The results show that the regression slopes between AMI and GEMS are more stable compared to the GEO-LEO ray-matching results. As VIIRS is a LEO sensor, the collocation thresholds need to be more relaxed, which leads to a wider range of regression slopes over time. Nevertheless, the GEO-LEO regression slopes are closer to unity, which confirms that GEMS has a positive bias of approximately 15% in its signals especially beyond 450 nm, necessitating a correction in its radiometric calibration coefficients. Most GEMS Level 2 products utilize reflective spectral features for retrieval, such as employing differential optical absorption spectroscopy (DOAS) (Platt & Stutz, 2008). While overall systematic bias across spectra may have minimal impact on retrieval under such approaches, it still has the potential to influence specific retrieval processes relying on theoretical irradiance for radiance scaling (Cho et al., 2023).

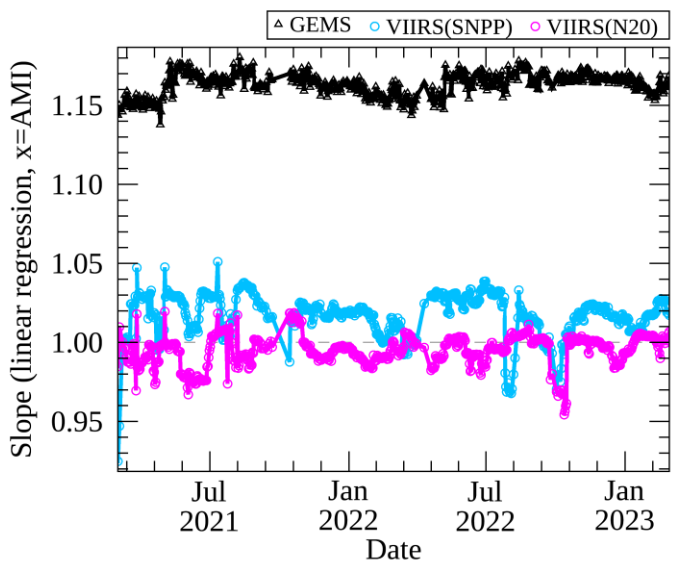

Figure 4. The regression slopes of reflectances derived from AMI with GEMS (black triangles) and VIIRS onboard Suomi-NPP and NOAA-20 (blue and magenta circles, respectively). The data is collected from March 2021 to February 2023 at daily intervals.

3.2.2 Diurnal variation

The GEO-GEO inter-calibration offers unique insights into diurnal variation of measured signals, which are not as readily available through the GEO-LEO comparison. Table 1 presents the statistics of AMI and GEMS radiances measured in 2021 at different observation times (01-06 UTC) with correlation coefficient, regression slope, bias, and root mean square error (RMSE).

There is a decreasing trend in both regression slope and bias, which is similarly observed in reflectance (not shown) across different seasons and surface types (land or ocean). This indicates there is a consistent diurnal influence in the comparison results of AMI and GEMS. Although the cause of this temporal dependence remains unclear, it may stem from various factors, including angle dependence as discussed in Section 3.1.2. The results emphasize the potential of the GEO-GEO inter-calibration in enhancing our understanding of temporal fluctuations, thereby possibly refining inter-calibration methodologies in future research.

Table 1. *Statistics of AMI and GEMS Radiances Measured in 2021 at Different observation Times Ranging from 1 to 6 UTC*

UTC	Correlation coefficient	Slope	Bias [W cm^{-3} sr^{-1}]	RMSE [W cm^{-3} sr^{-1}]
1 (10 KST)	0.987	1.107	13.3	25.8
2 (11 KST)	0.984	1.104	13.6	27.4
3 (12 KST)	0.981	1.101	13.6	28.6
4 (13 KST)	0.982	1.099	13.3	27.1
5 (14 KST)	0.985	1.099	12.4	25.8
6 (15 KST)	0.984	1.099	10.8	22.9

4 Conclusions

This research introduces an inter-calibration method, specifically utilizing ray-matching, to compare and monitor Level 1B products between instruments onboard twin satellites, GEMS/GK2B and AMI/GK2A. The close alignment of their sub-nadir positions offers a practical advantage, enabling matched optical viewing paths and generating extensive collocation datasets that cover a broad range of observation conditions.

With the datasets over two years, we conducted comprehensive spatial and temporal analyses between AMI and GEMS. The spatial analysis successfully addressed the calibration update of GEMS for solar irradiance and reflectance, though signal and scattering angle dependencies underscore the necessity for further analysis. Temporal analysis highlighted sensor drifts in regression slopes and radiometric calibration uncertainties in GEMS while emphasizing the significance of diurnal variation studies.

Our findings emphasize the critical role of GEO-GEO inter-calibration in enhancing our understanding of the measurement characteristics. Future investigations should focus on identifying the root causes of observed dependencies and biases, thereby advancing the effectiveness of inter-calibration techniques. This study aims to inform and facilitate future research endeavors, potentially aiding in the monitoring of sensors in similar configurations, such as the Flexible Combined Imager (FCI) and Sentinel-4.

Acknowledgments

This research has been supported by the Basic Science Research Program through the National Research Foundation of Korea (NRF) funded by the Ministry of Education (grant no. 2018R1A6A1A08025520).

Open Research

The AMI Level 1B products are available at https://datasvc.nmsc.kma.go.kr/datasvc/html/main/main.do?lang=en. The AMI SRFs for all channels and land sea mask are also available at https://datasvc.nmsc.kma.go.kr/datasvc/html/base/cmm/selectPage.do?page=static.software. The GSICS inter-calibration coefficients between AMI and VIIRS were provided by NMSC, and the coefficients can be reproduced by applying the methodology described in D. Kim et al. (2021). The GEMS Level 1C products can be accessed through the SFTP service provided by the Environmental Satellite Center (ESC) of the National Institute of Environmental Research (NIER) (https://nesc.nier.go.kr/en/html/cntnts/91/static/page.do), following approval from the institute. The datasets are not publicly available so far due to the regulation of the institution for the Level 1C products, and the datasets are accessible to researchers only volunteering on the GEMS calibration and validation project. The MATLAB code for the weighted regression algorithm is freely available at https://www.npl.co.uk/resources/software/iso-ts-28037-2010e.

References

Alsweiss, S. O., Jelenak, Z., Chang, P. S., Park, J. D., & Meyers, P. (2015). Inter-calibration Results of the Advanced Microwave Scanning Radiometer-2 Over Ocean. IEEE Journal of Selected Topics in Applied Earth Observations and Remote Sensing, 8(9), 4230–4238. https://doi.org/10.1109/JSTARS.2014.2330980

Chander, G., Hewison, T. J., Fox, N., Wu, X., Xiong, X., & Blackwell, W. J. (2013). Overview of intercalibration of satellite instruments. IEEE Transactions on Geoscience and Remote Sensing, 51(3), 1056–1080. https://doi.org/10.1109/TGRS.2012.2228654

Cho, Y., Kim, J., Go, S., Kim, M., Lee, S., Kim, M., et al. (2023). First Atmospheric Aerosol Monitoring Results from Geostationary Environment Monitoring Spectrometer (GEMS) over Asia. Atmospheric Measurement Techniques Discussions, 2023, 1–29. https://doi.org/10.5194/amt-2023-221

Choi, W. J., Moon, K.-J., Yoon, J., Cho, A., Kim, S., Lee, S., et al. (2019). Introducing the geostationary environment monitoring spectrometer. Journal of Applied Remote Sensing, 13(01), 1. https://doi.org/10.1117/1.jrs.13.019901

Doelling, D. R., Morstad, D., Scarino, B. R., Bhatt, R., & Gopalan, A. (2013). The Characterization of Deep Convective Clouds as an Invariant Calibration Target and as a Visible Calibration Technique. IEEE Transactions on Geoscience and Remote Sensing, 51(3), 1147–1159. https://doi.org/10.1109/TGRS.2012.2225066

Doelling, D. R., Haney, C. O., Scarino, B. R., Gopalan, A., & Bhatt, R. (2016). Improvements to the Geostationary Visible Imager Ray-Matching Calibration Algorithm for CERES Edition 4. Journal of Atmospheric and Oceanic Technology, 33(12), 2679–2698. https://doi.org/10.1175/JTECH-D-16-0113.1

Hewison, T. J. (2013). An Evaluation of the Uncertainty of the GSICS SEVIRI-IASI Intercalibration Products. IEEE TRANSACTIONS ON GEOSCIENCE AND REMOTE SENSING, 51(3). https://doi.org/10.1109/TGRS.2012.2236330

Hu, Y., Wielicki, B. A., Yang, P., Stackhouse, P. W., Lin, B., & Young, D. F. (2004). Application of Deep Convective Cloud Albedo Observation to Satellite-Based Study of the Terrestrial Atmosphere: Monitoring the Stability of Spaceborne Measurements and Assessing Absorption Anomaly. IEEE TRANSACTIONS ON GEOSCIENCE AND REMOTE SENSING, 42(11). https://doi.org/10.1109/TGRS.2004.834765

International Organization for Standardization Technical Specification (ISO/TS). (2010). ISO 28037:2010 Determination and Use of Straight-line Calibration Functions. Geneva, Switzerland: International Organization for Standardization (ISO). Retrieved from https://www.iso.org/standard/44473.html

Jiang, G.-M., Yan, H., & Ma, L.-L. (2009). Intercalibration of SVISSR/FY-2C Infrared Channels Against MODIS/Terra and AIRS/Aqua Channels; Intercalibration of SVISSR/FY-2C Infrared Channels Against MODIS/Terra and AIRS/Aqua Channels. IEEE Transactions on Geoscience and Remote Sensing, 47(5). https://doi.org/10.1109/TGRS.2008.2005200

Kang, M., Ahn, M. H., Liu, X., Jeong, U., & Kim, J. (2020). Spectral calibration algorithm for the geostationary environment monitoring spectrometer (Gems). Remote Sensing, 12(17), 1–17. https://doi.org/10.3390/rs12172846

Kang, M., Ahn, M. H., Ko, D. H., Kim, J., Nicks, D., Eo, M., et al. (2022). Characteristics of the Spectral Response Function of Geostationary Environment Monitoring Spectrometer Analyzed by Ground and In-Orbit Measurements. IEEE Transactions on Geoscience and Remote Sensing, 60. https://doi.org/10.1109/TGRS.2021.3091677

Kang, M., Ahn, M.-H., Lee, Y., Eo, M., & Kim, J. (2023, October 25). GEMS Performance and Lessons Learned [PowerPoint slides]. Committee on Earth Observation Satellites (CEOS) AC-VC-19/ACSG Joint Meeting. Retrieved from https://ceos.org/document_management/Virtual_Constellations/AC-VC/Meetings/AC-VC-19/presentations/Presentations%20PDF/2.%20Wed%2025%20Oct%202023%20-%20TRACE%20GASES%20AND%20AEROSOLS%20AIR%20QUALITY/We-14_Kang_GEMS_v1.pdf March 21, 2024

Kim, D., Gu, M., Oh, T.-H., Kim, E.-K., & Yang, H.-J. (2021). Introduction of the Advanced Meteorological Imager of Geo-Kompsat-2a: In-Orbit Tests and Performance Validation. Remote Sensing, 13(7), 1303. https://doi.org/10.3390/rs13071303

Kim, J., Jeong, U., Ahn, M. H., Kim, J. H., Park, R. J., Lee, H., et al. (2020). New era of air quality monitoring from space: Geostationary environment monitoring spectrometer (GEMS). Bulletin of the American Meteorological Society, 101(1), E1–E22. https://doi.org/10.1175/BAMS-D-18-0013.1

Lee, S. J., & Ahn, M.-H. (2021). Synergistic Benefits of Intercomparison Between Simulated and Measured Radiances of Imagers Onboard Geostationary Satellites. IEEE Transactions on Geoscience and Remote Sensing, 59(12), 10725–10737. https://doi.org/10.1109/TGRS.2021.3054030

Lee, Y., Ahn, M. H., & Kang, M. (2020). The new potential of deep convective clouds as a calibration target for a geostationary UV/VIS hyperspectral spectrometer. Remote Sensing, 12(3). https://doi.org/10.3390/rs12030446

Lee, Y., Ahn, M.-H., Kang, M., & Eo, M. (2023). Spectral replacement using machine learning methods for continuous mapping of the Geostationary Environment Monitoring Spectrometer (GEMS). Atmospheric Measurement Techniques, 16(1), 153–168. https://doi.org/10.5194/AMT-16-153-2023

Minnis, P., & Harrison, E. F. (1984). Diurnal Variability of Regional Cloud and Clear-Sky Radiative Parameters Derived from GOES Data. Part III: November 1978 Radiative Parameters. Journal of Applied Meteorology and Climatology, 23(7), 1032–1051. https://doi.org/10.1175/1520-0450(1984)023

Minnis, P., Young, D. F., & Harrison, E. F. (1991). Examination of the Relationship between Outgoing Infrared Window and Total Longwave Fluxes Using Satellite Data. Journal of Climate, 4(11), 1114–1133. https://doi.org/10.1175/1520-0442(1991)004<1114:EOTRBO>2.0.CO;2

Minnis, P., Nguyen, L., Doelling, D. R., Young, D. F., Miller, W. F., & Kratz, D. P. (2002a). Rapid Calibration of Operational and Research Meteorological Satellite Imagers. Part I: Evaluation of Research Satellite Visible Channels as References. Journal of Atmospheric and Oceanic Technology, 19(9), 1233–1249. https://doi.org/10.1175/1520-0426(2002)019<1233:RCOOAR>2.0.CO;2

Minnis, P., Nguyen, L., Doelling, D. R., Young, D. F., Miller, W. F., & Kratz, D. P. (2002b). Rapid Calibration of Operational and Research Meteorological Satellite Imagers. Part II: Comparison of Infrared Channels. Journal of Atmospheric and Oceanic Technology, 19(9), 1250–1266. https://doi.org/10.1175/1520-0426(2002)019<1250:RCOOAR>2.0.CO;2

Minnis, P., Doelling, D. R., Nguyen, L., Miller, W. F., & Chakrapani, V. (2008). Assessment of the Visible Channel Calibrations of the VIRS on TRMM and MODIS on Aqua and Terra. Journal of Atmospheric and Oceanic Technology, 25(3), 385–400. https://doi.org/10.1175/2007JTECHA1021.1

National Physical Laboratory. (2014, November 17). Determination and use of straight-line calibration functions [Software]. NPL Resources. Retrieved from https://www.npl.co.uk/resources/software/iso-ts-28037-2010e.

Platt, U., & Stutz, J. (2008). Differential Absorption Spectroscopy. In Differential Optical Absorption Spectroscopy: Principles and Applications (pp. 135–174). Berlin, Heidelberg: Springer. https://doi.org/10.1007/978-3-540-75776-4_6

Saunders, R. W., Blackmore, T. A., Candy, B., Francis, P. N., & Hewison, T. J. (2013). Monitoring Satellite Radiance Biases Using NWP Models. IEEE Transactions on Geoscience and Remote Sensing, 51(3), 1124–1138. https://doi.org/10.1109/TGRS.2012.2229283

Sohn, B.-J., Ham, S.-H., & Yang, P. (2009). Possibility of the Visible-Channel Calibration Using Deep Convective Clouds Overshooting the TTL. Journal of Applied Meteorology and Climatology, 48(11), 2271–2283. https://doi.org/10.1175/2009JAMC2197.1

Sterckx, S., Livens, S., & Adriaensen, S. (2013). Rayleigh, Deep Convective Clouds, and Cross-Sensor Desert Vicarious Calibration Validation for the PROBA-V Mission. IEEE Transactions on Geoscience and Remote Sensing, 51(3), 1437–1452. https://doi.org/10.1109/TGRS.2012.2236682

Wang, L., Cao, C., & Goldberg, M. (2009). Intercalibration of GOES-11 and GOES-12 Water Vapor Channels with MetOp IASI Hyperspectral Measurements. Journal of Atmospheric and Oceanic Technology, 26(9), 1843–1855. https://doi.org/10.1175/2009JTECHA1233.1

Wang, M. (2016). Rayleigh radiance computations for satellite remote sensing: accounting for the effect of sensor spectral response function. Opt. Express, 24(11), 12414–12429. https://doi.org/10.1364/OE.24.012414

Xiong, X., Angal, A., Chang, T., Chiang, K., Lei, N., Li, Y., et al. (2020). MODIS and VIIRS Calibration and Characterization in Support of Producing Long-Term High-Quality Data Products. Remote Sensing 2020, Vol. 12, Page 3167, 12(19), 3167. https://doi.org/10.3390/RS12193167

Zoogman, P., Liu, X., Suleiman, R. M., Pennington, W. F., Flittner, D. E., Al-Saadi, J. A., et al. (2017). Tropospheric emissions: Monitoring of pollution (TEMPO). Journal of Quantitative Spectroscopy and Radiative Transfer, 186, 17–39. https://doi.org/https://doi.org/10.1016/j.jqsrt.2016.05.008